JACS
JOURNAL OF THE AMERICAN CHEMICAL SOCIETY
Article
pubs.acs.org/JACS

High-Performance Electrocatalysis Using Metallic Cobalt Pyrite (CoS_2) Micro- and Nanostructures

Matthew S. Faber, Rafal Dziedzic, Mark A. Lukowski, Nicholas S. Kaiser, Qi Ding, and Song Jin*

Department of Chemistry, University of Wisconsin—Madison, 1101 University Avenue, Madison, Wisconsin 53706, United States

Supporting Information

ABSTRACT: The development of efficient and robust earth-abundant electrocatalysts for the hydrogen evolution reaction (HER) is an ongoing challenge. We report metallic cobalt pyrite (cobalt disulfide, CoS_2) as one such high-activity candidate material and demonstrate that its specific morphology—film, microwire, or nanowire, made available through controlled synthesis—plays a crucial role in determining its overall catalytic efficacy. The increase in effective electrode surface area that accompanies CoS_2 micro- and nanostructuring substantially boosts its HER catalytic performance, with CoS_2 nanowire electrodes achieving geometric current densities of -10 mA cm^{-2} at overpotentials as low as -145 mV vs the reversible hydrogen electrode. Moreover, micro- and nanostructuring of the CoS_2 material has the synergistic effect of increasing its operational stability, cyclability, and maximum achievable rate of hydrogen generation by promoting the release of evolved gas bubbles from the electrode surface. The benefits of catalyst micro- and nanostructuring are further demonstrated by the increased electrocatalytic activity of CoS_2 nanowire electrodes over planar film electrodes toward polysulfide and triiodide reduction, which suggests a straightforward way to improve the performance of quantum dot- and dye-sensitized solar cells, respectively. Extension of this micro- and nanostructuring strategy to other earth-abundant materials could similarly enable inexpensive electrocatalysts that lack the high intrinsic activity of the noble metals.

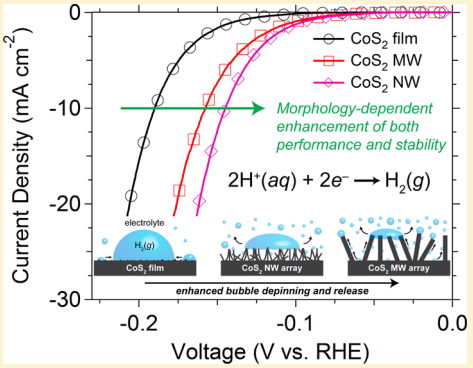

INTRODUCTION

The promise of hydrogen as a sustainable, secure, and clean alternative energy carrier that can satisfy the growing global energy demand will be realized only through its efficient, low-cost, and environmentally friendly production.[1,2] Water electrolysis to give hydrogen fuel—preferably driven by solar energy—is a highly attractive means for meeting these requirements.[3−7] Among the many hydrogen evolution reaction (HER) electrocatalysts, noble metals such as platinum are the best,[8] but scarcity and high cost limit their applicability.[9] Identifying and developing high-performance earth-abundant substitutes for these precious metal electrocatalysts serves as one pathway toward enabling a hydrogen economy.[10−24] Expanding their anticipated scope of utility, such earth-abundant electrocatalysts may also serve as replacements for noble metals in catalyzing the electrochemical reactions central to other emerging renewable energy technologies, such as polysulfide and triiodide reduction in quantum dot-sensitized solar cells (QDSSCs)[25,26] and dye-sensitized solar cells (DSSCs),[27] respectively.

The pyrite-phase transition metal dichalcogenides (MX_2, where typically M = Fe, Co, or Ni and X = S or Se) are common minerals that have seldom been explored for electrocatalysis despite past suggestion that they could be efficient HER catalysts.[28] They are of particular interest due to their extremely low cost and expected long-term stability in both acidic and alkaline operating environments. Lately, there has been renewed activity in pyrite-phase electrocatalyst research.[23,24,29,30] When prepared as thin films on glassy carbon or as nanoparticles supported by carbon black, these pyrite-phase electrocatalysts exhibit encouraging HER activity.[23,30] This activity has been further enhanced by synthesizing nanoparticles on high surface area carbon fiber paper.[24] In particular, among these pyrite-phase transition metal dichalcogenides, cobalt pyrite (cobalt disulfide, CoS_2; cattierite) is intrinsically a conductive metal—in contrast to the semiconducting pyrites, such as nickel disulfide[31] or iron disulfide[32,33]—making it uniquely advantaged as an electrocatalyst material. Metallically conducting thin films of CoS_2 with a reported sheet resistance of 19.2 ± 0.3 Ω sq^{-1} prepared directly on insulating plate glass substrates have been previously demonstrated to be highly effective counter electrodes for QDSSCs that employ the aqueous sulfide/polysulfide redox electrolyte.[29] Similarly, CoS_2 has recently been identified as an efficient electrocatalyst for oxygen reduction.[34−36] Importantly, as a stable, intrinsically metallic mineral, CoS_2 possesses clear advantages over the more prominent layered transition metal dichalcogenide electrocatalysts, such as MoS_2[10−13] and WS_2,[16,17] that exhibit high activity toward the HER only after conversion from their thermodynamically favored semiconducting phase to a metastable metallic polymorph.[10,12,13,16,17]

Received: April 24, 2014
Published: June 5, 2014

   dx.doi.org/10.1021/ja504099w | J. Am. Chem. Soc. 2014, 136, 10053−10061

Furthermore, the performance of promising earth-abundant HER electrocatalysts could be enhanced through nanostructuring, as recently shown for MoS_2,[10−13] amorphous MoS_x,[15] WS_2,[16,17] Ni_2P,[18] CoP,[19] and Ni−Mo alloys.[20,21] With the increasing roughness (i.e., the total surface area relative to the geometric surface area) that accompanies decreasing structure size, the number of available catalytic sites is expected to increase, thereby relaxing the stringent requirements of intrinsic catalytic activity required to achieve a specified level of performance. Moreover, compared with the common high surface area nanoparticle and nanostructured film morphologies, arrays of catalytic micro- and nanowires (MWs and NWs, respectively) directly integrated with a conducting electrode could enjoy the additional advantages of further enhanced performance and improved stability by facilitating both charge carrier transport[10] and the release of evolved hydrogen gas from the electrode surface.[37] In this work, we establish CoS_2 as a high-performance, earth-abundant electrocatalyst material for the HER. We further develop facile routes for CoS_2 MW and NW growth in high density directly on graphite substrates and show their dramatically improved performance and stability (particularly for the MW electrodes) during HER electrocatalysis. The generality of these syntheses also permits the preparation of CoS_2 MWs and NWs on glass substrates and the demonstration of their increased activity toward polysulfide and triiodide reduction, which could boost QDSSC and DSSC performance, respectively, without using noble metal electrodes.

■ MATERIALS AND METHODS

Full synthesis and characterization details appear in the Supporting Information.

Materials Synthesis. *CoS_2 Films.* The CoS_2 films were synthesized on graphite and glass substrates by electron-beam evaporating 100 nm of Co (Kurt J. Lesker, 99.95%) onto the substrate at 1 Å s^{-1} and then thermally sulfidizing the Co film.

CoS_2 Microwires. Cobalt hydroxide (β-$Co(OH)_2$) MWs were synthesized on graphite and glass substrates using a published procedure with minor modifications.[38,39] In a typical synthesis, 10 mmol of $Co(NO_3)_2{\cdot}6H_2O$ (Sigma-Aldrich, ≥98%) was dissolved in 10 mL of 18.2 MΩ cm distilled water. Then, 40 mL of concentrated NH_4OH(aq) solution (Sigma-Aldrich, 28.0−30.0%) was added dropwise to the stirred solution. The solution was stirred in ambient air for 30 min before adding 16 mL to a 23 mL Teflon (PTFE) autoclave liner containing the substrate. The reaction vessel was loosely covered with a watch glass and heated at 85 °C for 14 h in a ventilated forced-air convection oven. After 14 h, the substrate was removed, rinsed, and dried under a stream of nitrogen. The β-$Co(OH)_2$ MWs were then thermally sulfidized to give CoS_2 MWs.

CoS_2 Nanowires. Cobalt hydroxide carbonate hydrate ($Co(OH)(CO_3)_{0.5}{\cdot}xH_2O$, "CHCH") NWs were synthesized on graphite and glass substrates by following a published procedure with minor modifications.[40] In a typical synthesis, 1.5 mmol of $Co(NO_3)_2{\cdot}6H_2O$, 3 mmol of NH_4F (Sigma-Aldrich, ≥98.0%), and 7.5 mmol of $(NH_2)_2CO$ (Riedel-de Haën, 99.5−100.5%) were dissolved in 50 mL of distilled water. Then, 16 mL of this solution was transferred to a 23 mL PTFE-lined stainless steel autoclave containing the substrate, which was sealed and heated at 110 °C for 5 h. After cooling, the substrate was removed, rinsed, and dried under a stream of nitrogen. The CHCH NWs were then thermally sulfidized to give CoS_2 NWs.

Thermal Sulfidation. The as-prepared Co films, β-$Co(OH)_2$ MWs, and CHCH NWs on graphite or glass were thermally sulfidized to CoS_2 using a previously described procedure.[29] Briefly, the substrates covered with precursor material were placed in the center of a fused silica tube on a reactor equipped with both pressure and gas flow controllers. An alumina boat containing 2 g of S powder (Sigma-Aldrich, 99.5−100.5%) was placed in the tube at the farthest upstream position within the tube furnace. The tube was purged of air and maintained at 780 Torr under a steady flow of Ar carrier gas (99.999%) at 25 sccm. The furnace temperature was ramped to 500 °C and held for 1 h. After cooling under Ar flow, the samples were rinsed with CS_2 (Sigma-Aldrich, 99.9%) and dried with nitrogen.

Materials Characterization. The as-prepared films, MWs, and NWs on graphite or glass were characterized using a LEO SUPRA 55 VP field-emission scanning electron microscope (SEM) operated at 2 kV and a Bruker D8 ADVANCE powder X-ray diffractometer (XRD) using Cu Kα radiation. The XRD pattern background was fit to a cubic spline and subtracted using Jade 5 (Materials Data, Inc.). Transmission electron microscopy (TEM) samples were prepared by dispersing as-prepared MWs on graphite in isopropyl alcohol by ultrasonication (100 W, 10 s) and drop casting the suspended MWs onto the lacey carbon support of a Cu grid (Ted Pella, 01890-F). High-resolution TEM images of the β-$Co(OH)_2$ and CoS_2 MWs were obtained on an aberration-corrected FEI Titan scanning transmission electron microscope operated at an accelerating voltage of 200 kV in TEM mode. Raman spectra of the as-prepared and as-measured CoS_2 film on graphite were collected on a Thermo Scientific DXR Raman microscope fitted with 532 nm excitation laser. X-ray photoelectron spectroscopy (XPS) was performed on as-synthesized and as-measured CoS_2 films on graphite using a Thermo Scientific K-Alpha XPS system with an Al Kα source.

Electrochemical Characterization of Catalytic Activity toward the HER. All electrochemical measurements were performed in a three-electrode configuration using a rotating disk electrode (RDE) setup (Bioanalytical Systems, Inc.; RDE-2) and recorded using a Bio-Logic SP-200 potentiostat. Each measurement was performed in room-temperature 0.5 M H_2SO_4(aq) electrolyte continuously purged with H_2(g) (99.999%) using a saturated calomel reference electrode (SCE) (CH Instruments), a graphite rod (National Carbon Co., AGKSP Spectroscopic Electrode) as the counter electrode, and a graphite-supported CoS_2 film, MW array, or NW array affixed to a glassy carbon RDE tip using silver paint (Ted Pella, PELCO Colloidal Silver) as the working electrode. Linear sweep or cyclic voltammograms were measured a minimum of five times from +0.25 to −0.45 V vs the reversible hydrogen electrode (RHE) (+0.25 to −0.24 V vs RHE for film electrodes) at a scan rate of 3 mV s^{-1} in both the forward and reverse directions while rotating the working electrode at 2000 rpm, with the final sweep always used for analysis. The SCE was calibrated against the reversible hydrogen potential using platinum wire (Kurt J. Lesker, 99.99%; 0.50 mm diameter) as both the working and counter electrodes after each measurement. The Pt reference trace was recorded using a Pt wire as the working electrode. All polarization curves were corrected for background current and *IR* losses, as detailed in the Supporting Information, unless otherwise noted. Electrochemical impedance spectroscopy was performed in potentiostatic mode at −0.24 V vs RHE, applying a sinusoidal voltage

dx.doi.org/10.1021/ja504099w | J. Am. Chem. Soc. 2014, 136, 10053−10061

with an amplitude of 10 mV and scanning frequency from 200 kHz to 50 mHz.

Symmetrical Cell Fabrication and Measurement. The electrochemical symmetrical cells were fabricated and characterized by following a published procedure with minor modifications.[29] The sulfide/polysulfide electrolyte consisted of 2 M $Na_2S{\cdot}9H_2O$ (Sigma-Aldrich, ≥99.99%) and 2 M S in aqueous solution. The iodide/triiodide electrolyte consisted of 0.6 M 1-methyl-3-propylimidazolium iodide (Solaronix SA; "PMII")/0.03 M I_2 (Sigma-Aldrich, ≥99.8%)/0.1 M guanidinium thiocyanate (Sigma-Aldrich, ≥97%; "GSCN")/0.5 M 4-*tert*-butylpyridine (Fluka, >98%; "TBP") in 85:15 (v/v) acetonitrile (Sigma-Aldrich, anhydrous, 99.8%; "ACN"):valeronitrile (Sigma-Aldrich, 99.5%; "VN").

RESULTS AND DISCUSSION

The different routes for preparing CoS_2 film, MW array, and NW array electrodes are summarized in Figure 1. CoS_2 films

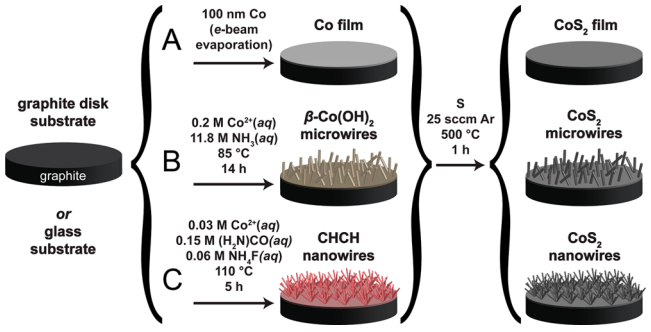

Figure 1. Schematic depictions of the preparation of a cobalt pyrite (CoS_2) film, microwire (MW) array, or nanowire (NW) array on a graphite disk (or glass) substrate. (A) The CoS_2 film is synthesized via the thermal sulfidation of a 100 nm thick cobalt film deposited on the substrate by electron-beam evaporation. (B) Cobalt hydroxide (β-$Co(OH)_2$) MWs are grown directly on the substrate from aqueous solution and then thermally sulfidized to give vertically oriented CoS_2 MWs. (C) Vertically oriented cobalt hydroxide carbonate hydrate ($Co(OH)(CO_3)_{0.5}{\cdot}xH_2O$, "CHCH") NWs are grown via hydrothermal synthesis directly on the substrate and then thermally sulfidized to give CoS_2 NWs in high density. The thermal sulfidation conditions are identical in each synthesis.

are synthesized directly on graphite (or glass) substrates via thermal sulfidation of a cobalt metal precursor film, as illustrated in Figure 1A. To prepare CoS_2 MWs and NWs, we first grow β-$Co(OH)_2$ MWs[38,39] or CHCH NWs[40] from solution directly on graphite (or glass) substrates, as shown schematically in Figure 1B and C, respectively. Then, these intermediate structures are converted to CoS_2 with complete retention of their one-dimensional morphology. The thermal sulfidation conditions are identical in all preparations (Figure 1), regardless of the intermediate material. Prior to thermal sulfidation, the β-$Co(OH)_2$ MWs and CHCH NWs can both be optionally converted to a cobalt oxide (Co_3O_4) intermediate by dehydration in air or inert atmosphere at 350 °C for 2 h, but this additional step was not found to impact the final CoS_2 MW or NW morphology or performance. The graphite disk substrate was selected as a convenient, low-cost, chemically inert, electrically conductive support that has negligible activity toward the HER and is insensitive to the harsh conditions of the thermal sulfidation. The direct growth of CoS_2 on graphite substrates ensures a low-resistance electrical contact between the substrate and the electrocatalyst to minimize *IR* losses.[10] Note that metallically conducting CoS_2 films, MW arrays, and NW arrays can also be prepared directly on insulating glass substrates using the same synthetic procedures (Figure S1, Supporting Information).

Scanning electron microscopy (SEM) shows that, upon thermal sulfidation, the 100 nm thick evaporated Co film on graphite (Figure 2A) converts to a polycrystalline CoS_2 film

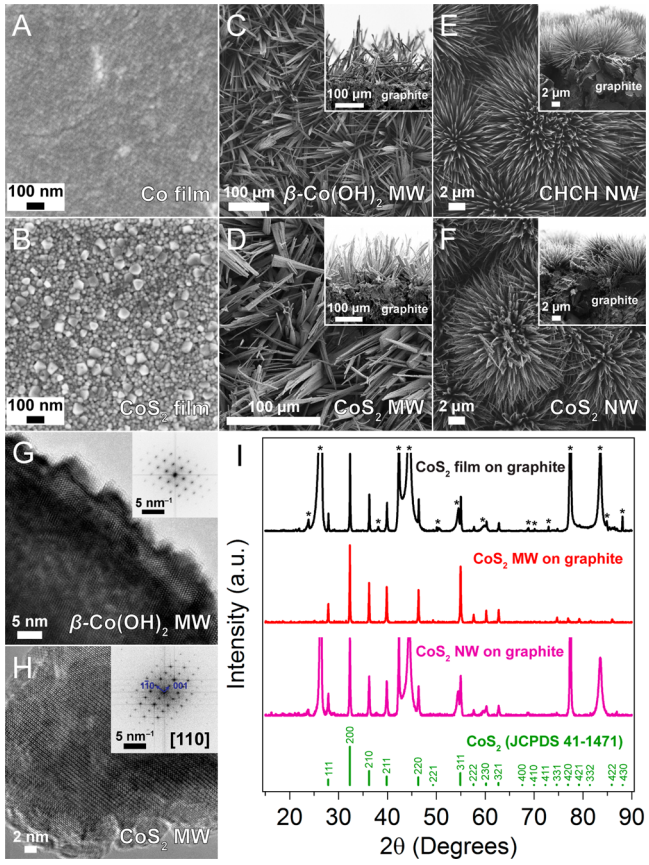

Figure 2. Structural characterization of an as-synthesized CoS_2 film, MW array, and NW array on graphite and their corresponding precursors. SEM images of (A) an evaporated Co film, (B) a polycrystalline CoS_2 film, (C) cobalt hydroxide (β-$Co(OH)_2$) MWs, (D) CoS_2 MWs, (E) cobalt hydroxide carbonate hydrate ($Co(OH)(CO_3)_{0.5}{\cdot}xH_2O$, "CHCH") NWs, and (F) CoS_2 NWs on graphite (with cross-sectional SEM images inset in the corresponding panels). High-resolution TEM images of the as-synthesized (G) β-$Co(OH)_2$ and (H) CoS_2 MW products and the corresponding fast Fourier transforms (inset) confirm their crystallinity and phase. (I) XRD patterns of the as-synthesized CoS_2 film (black trace), MW array (red trace), and NW array (violet trace) products on graphite compared with the standard pattern for CoS_2 (JCPDS 41-1471). The high-intensity reflections from the graphite substrate are truncated and indicated by asterisks above the CoS_2 film pattern.

with grain sizes of approximately 20−80 nm (Figure 2B). While this preparation yields a film that completely covers the graphite surface, large pits and imperfections in the graphite disk itself typically remain visible (Figure S2, Supporting Information). On the other hand, the solution synthesis of the β-$Co(OH)_2$ MWs and CHCH NWs tends to fill in these imperfections, resulting in a surface topography that is dominated by the MW or NW products (Figure 2C−F). In these syntheses, the early formation of a conformal particulate

dx.doi.org/10.1021/ja504099w | J. Am. Chem. Soc. 2014, 136, 10053−10061

β-$Co(OH)_2$ or CHCH film over the graphite substrate is observed (inset cross-sectional SEM images of Figure 2C and E, respectively), and especially in the case of β-$Co(OH)_2$, this defective film likely seeds one-dimensional screw dislocation-driven MW or NW growth.[39,41] The intimate integration of the β-$Co(OH)_2$ and CHCH products with the graphite surface could also impart enhanced mechanical stability. The β-$Co(OH)_2$ MWs vary in diameter over approximately 5−30 μm, and their lengths generally exceed 100 μm (Figure 2C). The β-$Co(OH)_2$ synthesis strongly favors the formation of long, thick MWs, particularly on graphite substrates; however, we very occasionally observed the growth of shorter, thinner β-$Co(OH)_2$ MWs or NWs, which is actually the more common product morphology on glass substrates (Figure S1, Supporting Information). The CHCH NWs have a fairly consistent diameter of approximately 100 nm, and they densely grow in radial sea urchin-like structures with lengths around 10 μm (Figure 2E). The phase and phase purity of these as-synthesized intermediate products have been confirmed by XRD analysis (Figure S3, Supporting Information). Upon thermal sulfidation, the β-$Co(OH)_2$ MWs and CHCH NWs are fully converted to CoS_2 with retention of their one-dimensional morphology, albeit with an apparent increase in surface roughness likely owing to grain growth (Figure 2D and F). High-resolution TEM further confirmed the crystallinity and phase of the as-synthesized β-$Co(OH)_2$ and CoS_2 MW products (Figure 2G and H, respectively). The fast Fourier transform (FFT) inset in Figure 2H is indexed to the [110] zone axis of CoS_2. XRD analysis of the as-prepared CoS_2 film, MW, and NW products on graphite confirms the overall phase purity of the conversion products (Figure 2I), with all peaks corresponding to CoS_2 (JCPDS 41-1471; space group $Pa\bar{3}$; a = 5.5376 Å) with no preferred orientation, perhaps consistent with the coarsening observed in the SEM images. Note that, in the XRD pattern for the CoS_2 MWs, reflections from graphite are not visible due to heavy product coverage on the substrate.

The direct preparation of the CoS_2 films, MWs, and NWs on graphite allows for convenient evaluation of their electrocatalytic activity toward the HER by mounting the graphite disk on the glassy carbon working electrode of a standard RDE apparatus. All measurements of HER activity were performed in 0.5 M H_2SO_4(aq) electrolyte continuously purged with H_2(g) and were corrected for background current and *IR* losses unless otherwise indicated (Figure S4, Supporting Information). The origin of the background current (which has been previously observed for pyrite-phase HER electrocatalysts[23]) is complex, but it most likely results primarily from capacitive charging of the CoS_2 surface (Supporting Information). Polarization curves showing the geometric current density (J) plotted against the applied potential appear in Figure 3A for representative samples of the different CoS_2 morphologies, along with that of a Pt wire standard. It is important to note that the CoS_2 film electrodes were measured over a narrowed range of applied potentials as compared to the MW and NW electrodes. This is because at elevated cathodic overpotentials (η) and high current densities, rapid H_2(g) evolution damages the CoS_2 film and causes its delamination, as evidenced by SEM, XRD, and Raman analysis (Figure S5A−D, Supporting Information). Such CoS_2 film instability could be exacerbated by the stresses formed at the CoS_2−graphite interface during thermal sulfidation. Therefore, the high electrocatalytic performance of the CoS_2 film electrodes toward the HER cannot be maintained upon repeated cycling when applying η < −0.25 V vs RHE (Figure S5E, Supporting Information) due the damage caused by the rapid evolution of H_2(g) bubbles. Limiting η to permit only modest current densities, however, greatly improves the cyclability of the CoS_2 film electrodes.

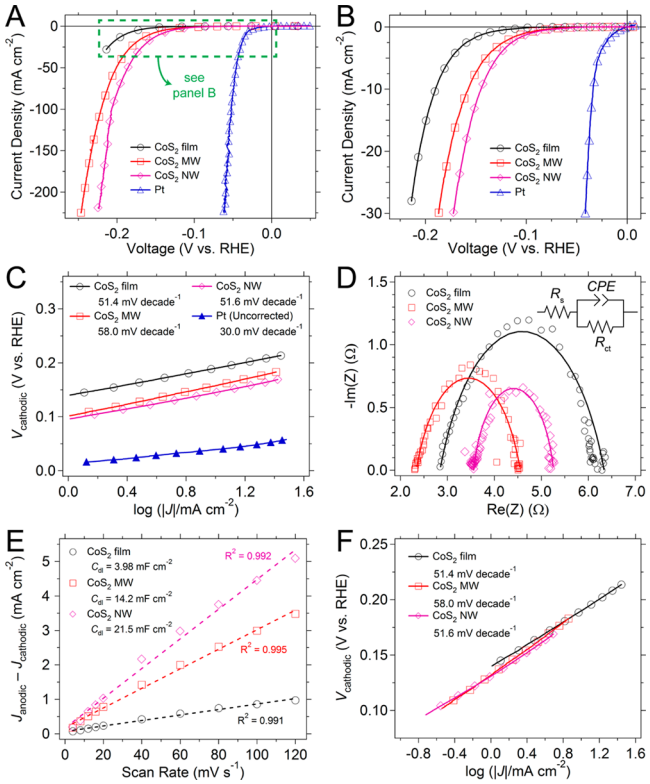

Figure 3. Electrochemical characterization of CoS_2 film, MW array, and NW array electrodes for HER electrocatalysis. Polarization curves at (A) higher and (B) lower applied overpotentials show the relative performance of the CoS_2 electrodes (film, open circles; MW, open squares; NW, open diamonds) in comparison to a Pt wire standard (open triangles). (C) Tafel analysis of the data presented in panels A and B. (D) Electrochemical impedance spectroscopy (EIS) Nyquist plots showing the similar series and operating charge transfer resistances of the different CoS_2 electrodes. The data was fit to the simplified Randles equivalent circuit shown in the inset, and the fitting results are shown as solid traces. (E) Plot showing the extraction of the double-layer capacitance (C_{dl}) for each CoS_2 electrode. (F) Tafel data from panel C normalized by relative electrode surface area to highlight the similar intrinsic activity of the CoS_2 electrodes.

Importantly, the comparison in Figure 3A shows that the CoS_2 catalyst morphology clearly plays a key role in its performance, with high current densities (i.e., $J_{cathodic}$ > 200 mA cm^{-2}) achievable only with the MW and NW samples. Figure 3B highlights this comparison over a range of moderate current densities and clearly shows the trend of decreasing overpotential required to achieve a target current density with increasing surface texture, in the order of film to MWs to NWs. Specifically, the CoS_2 film sample requires an applied overpotential of −190 mV vs RHE for significant H_2(g) evolution ($J_{cathodic}$ = 10 mA cm^{-2}), while the CoS_2 MW and NW array samples require only −158 and −145 mV vs RHE, respectively. These low overpotentials are among the best observed for non-noble metal HER electrocatalysts.[10−12,14−24] Moreover, the different CoS_2 electrodes all have a very low onset of cathodic current at around −75 mV vs RHE, which also compares favorably with that of other earth-abundant HER electrocatalysts.[10−12,14−24] This common onset potential

dx.doi.org/10.1021/ja504099w | J. Am. Chem. Soc. 2014, 136, 10053−10061

Table 1. Summary of the Electrochemical Properties of CoS_2 Electrodes with Different Morphologies

sample	η (mV vs RHE) for $J = -10$ mA cm^{-2}	R_{ct} (Ω cm^2)	Tafel slope (mV decade^{-1})	$J_{0,geometric}$ (μA cm^{-2})	C_{dl} (mF cm^{-2})	relative surface area	$J_{0,normalized}$ (μA cm^{-2})
CoS_2 film	−190	0.99	51.4	1.97	3.98	1.00	1.97
CoS_2 MW	−158	0.62	58.0	18.8	14.2	3.57	5.27
CoS_2 NW	−145	0.48	51.6	15.1	21.5	5.40	2.80

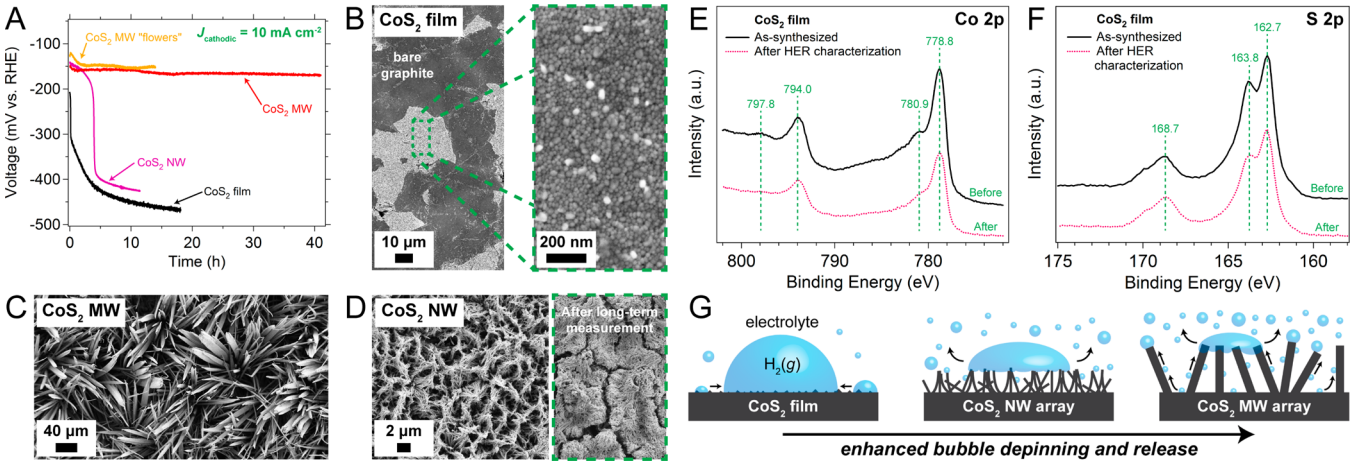

Figure 4. Characterization of CoS_2 stability during HER electrocatalysis and scheme illustrating enhanced hydrogen gas bubble release from CoS_2 nano- and microstructures. (A) Long-term stability measurements for representative CoS_2 film, NW, MW, and MW "flower" electrodes illustrating the greatly enhanced stability of the MW electrodes relative to the film and NW electrodes. SEM images of measured (B) CoS_2 film, (C) MW, and (D) NW electrodes. In the case of film electrodes (panel B), rapid $H_2(g)$ evolution can damage the film (left), but the remaining portions (magnified and highlighted by the dashed green box on the right) are relatively unchanged at the smaller length scale. Similarly, prolonged continuous measurement (>3 h) of the CoS_2 NW electrodes can result in NW breakage, cracking, and overall loss of the nanostructured morphology (dashed green box on the right of panel D). X-ray photoelectron spectra of the (E) Co 2p and (F) S 2p regions for as-synthesized (upper black traces) and electrochemically characterized (lower magenta traces) CoS_2 film electrodes. (G) Schematic depictions of CoS_2 NWs and MWs bursting the larger $H_2(g)$ bubbles that commonly pin at the CoS_2 film surface, with the MWs most effectively wicking the evolved bubbles and maintaining the solid–liquid interface.

suggests that, as expected for polycrystalline, phase-pure materials, there are no dramatic differences in the intrinsic activity of the different CoS_2 samples.

The Tafel slopes of the CoS_2 film, MW, and NW electrodes near the onset of substantial cathodic current are all in the approximate range of 50–60 mV decade^{-1}, with that of the film sample the lowest at 51.4 mV decade^{-1} (Figure 3C). While higher than the 30.0 mV decade^{-1} characteristic of Pt, these values compare quite favorably with the Tafel slopes of other recently reported high-performance earth-abundant HER electrocatalysts.[10−12,14−24] In particular, the similar Tafel slopes of the CoS_2 film, MW, and NW electrodes are roughly commensurate with a recent report on CoS_2 films, as are the geometric exchange current densities ($J_{0,geometric}$) calculated from these data (Table 1),[23] and again suggest that the disparity in performance is not due to variations in the intrinsic activity of the CoS_2 materials prepared through the different synthetic routes. Similarly, electrochemical impedance spectroscopy (EIS) analysis of these electrodes under operating conditions (i.e., at a cathodic bias that drives rapid hydrogen evolution) shows that the difference in their performance is likely not fully attributable to differences in the charge transfer resistance (R_{ct}) associated with $H_2(g)$ evolution (Figure 3D). The R_{ct} for each electrode was extracted by modeling the EIS data using a simplified Randles equivalent circuit (Figure 3D, inset). These fittings, shown as solid line traces through the measured data, yield geometric R_{ct} values of 0.99, 0.62, and 0.48 Ω cm^2 for the film, MW, and NW samples, respectively. Even though these R_{ct} values do follow the trend of increasing activity (Table 1), it is unlikely that a small variation in R_{ct} of ~0.5 Ω cm^2 fully accounts for the dramatic differences in observed performance. Additionally, the performance trend does not track with the amount of CoS_2 catalyst present, as the typical mass loading of the MW samples (25 ± 2 mg cm^{-2}) is much higher than that of the NW samples (1.7 ± 0.3 mg cm^{-2}) (Supporting Information). In an attempt to resolve this apparent discrepancy, we measured the capacitive current for the same CoS_2 samples as a function of scan rate in order to extract the double-layer capacitance (C_{dl}) of each electrode (Figure 3E), which serves as an estimate of the effective electrochemically active surface area of the solid–liquid interface (Figure S6, Supporting Information). By comparing these values of C_{dl}, the increase in relative effective surface area that results from micro- or nanostructuring of the CoS_2 material can be estimated, as shown in Table 1. This comparison reveals that the introduction of microstructuring to the CoS_2 material more than triples the effective surface area as compared to the CoS_2 film, while nanostructuring increases the effective surface area by over five times. It is likely this huge change in effective surface area that primarily accounts for the differences in performance, as evidenced by the fact that the current densities measured for the MW and NW samples similarly scale with their increased effective surface area over the range of low to moderate applied overpotentials. Indeed, when normalized by relative surface area, the Tafel data in Figure 3C are shifted such that they all fall on essentially the same Tafel line (Figure 3F) and yield similar normalized exchange current densities ($J_{0,normalized}$, Table 1), further suggesting the comparable

dx.doi.org/10.1021/ja504099w | J. Am. Chem. Soc. 2014, 136, 10053−10061

intrinsic activity of the CoS_2 materials, regardless of synthesis pathway.

In contrast to the limited performance of the CoS_2 films toward HER electrocatalysis, the CoS_2 MW and NW electrodes can be repeatedly cycled to pass extremely high cathodic currents with no losses and, in fact, often even improvements in their performance (Figure S7, Supporting Information), possibly due to the removal of surface contaminants or inactive surface species upon $H_2(g)$ evolution. Furthermore, the CoS_2 MW electrodes can maintain constant $H_2(g)$ evolution at $J_{cathodic}$ = 10 mA cm^{-2} with minimal change in the applied overpotential, as shown in Figure 4A (red trace). Over the duration of a 41-h stability measurement, the cathodic overpotential required for the CoS_2 MW electrode to maintain $J_{cathodic}$ = 10 mA cm^{-2} was very stable, increasing by only about 20 mV. SEM images of the CoS_2 film, MW, and NW electrodes after typical electrochemical characterization (Figure 4B–D) were also obtained to assess possible morphological and surface changes as a result of HER electrocatalysis. No noticeable changes in the appearance of the MW electrode can be detected (Figure 4C). On the other hand, the corresponding overpotential for the CoS_2 film electrode rapidly increased (Figure 4A, black trace), with a large jump occurring within 1 h, likely caused by the delamination and physical loss of electrocatalyst material, as shown in Figure 4B and further illustrated in Figure S5 of the Supporting Information. The CoS_2 NW electrodes showed improved stability relative to the film electrodes during conditions of continuous hydrogen evolution, but they eventually also suffered from the physical loss of CoS_2 material, as indicated by the sharp increase in overpotential after approximately 3 h (Figure 4A, violet trace). The CoS_2 NWs collapse and bundle up due to surface tension (Figure 4D, left) and tend to crack, break, and eventually separate from the graphite support after prolonged continuous operation (Figure 4D, right), leading to a drop in electrode performance after several hours. However, aside from the mechanical delamination of the films and eventual cracking of the NW arrays, at the nanoscale, the CoS_2 materials after typical HER electrochemical testing have essentially the same appearance (Figure 4B, right) as the as-synthesized products (Figure 2), suggesting the chemical robustness of the CoS_2 electrocatalyst. To further assess the chemical stability and oxidation states of CoS_2 under HER electrocatalysis conditions, X-ray photoelectron spectroscopy (XPS) was performed on CoS_2 films on graphite before and after electrochemical characterization (Figure 4E and F). The positions and relative intensities of the Co 2p (Figure 4E) and S 2p (Figure 4F) peaks, which are in good agreement with previous reports,[34,42] remain essentially unchanged as a result of HER electrocatalysis, suggesting the high chemical stability of CoS_2. The satellite peaks at 780.9 and 797.8 eV in the Co 2p spectrum (Figure 4E), as well as the sulfate peak at 168.7 eV in the S 2p spectrum (Figure 4F), indicate that CoS_2 is susceptible to oxidation in air, but these oxide products are removed upon exposure to the 0.5 M H_2SO_4(aq) electrolyte.

We believe that both the enhanced catalytic performance and stability when passing high current densities derive from the micro- or nanostructuring of the CoS_2 material. This is because when the production of $H_2(g)$ bubbles is vigorous ($J_{cathodic}$ > 10 mA cm^{-2}), the MWs and, to a lesser degree, NWs are superior in facilitating bubble convection away from the electrode surface (Figure 4G). Such behavior prevents the $H_2(g)$ bubbles from accumulating and damaging the catalyst, as commonly occurs for the CoS_2 films (Figure S5, Supporting Information, and earlier discussion), enabling the improved cyclability and long-term stability of the MW and NW electrodes. The improved integration of the MW and NW products with the graphite support may also contribute to their increased stability. Furthermore, for the CoS_2 films, large bubbles commonly pin at the electrode surface, reducing the effective electrode surface area;[37] on the other hand, we found that the CoS_2 NWs and, in particular, MWs tend to burst these larger bubbles and wick them away from the electrode surface (Figure 4G), much like air bubbles at the microstructured surface of a lotus leaf.[43] Still photographs of a CoS_2 MW electrode operating at $J_{cathodic}$ > 200 mA cm^{-2} reveal the efficiency with which the MWs suppress $H_2(g)$ bubble pinning, resulting in an electrolyte solution that is effectively turbid with numerous small bubbles cast off of the MW electrode (Figure S8, Supporting Information). Consistent with air bubble behavior at micro- and nanostructured silicon surfaces,[43] we have observed that the CoS_2 MW electrodes are most effective in promoting gas bubble release. Most importantly, conveyance of the $H_2(g)$ bubbles away from the electrode surface maintains the integrity of the solid–liquid interface necessary for HER electrocatalysis,[37] which, in addition to the concomitant increase in surface area that accompanies micro- and nanostructuring, may also be responsible for the improved performance of the MW and NW electrodes. In contrast, nanoparticulate or mesoporous electrocatalyst films can also enable increased effective electrode surface area, but they lack a mechanism to promote gas bubble release, which could result in mechanical instability and decreased performance at high current densities, as has been observed for the CoS_2 film electrodes.

The synergistic effects of a large electrode surface area and a microstructured morphology to promote $H_2(g)$ bubble release is best demonstrated by the hierarchical CoS_2 MW "flower" samples that we sometimes obtained on graphite via the β-$Co(OH)_2$ MW synthesis route (Figure 5A and additional

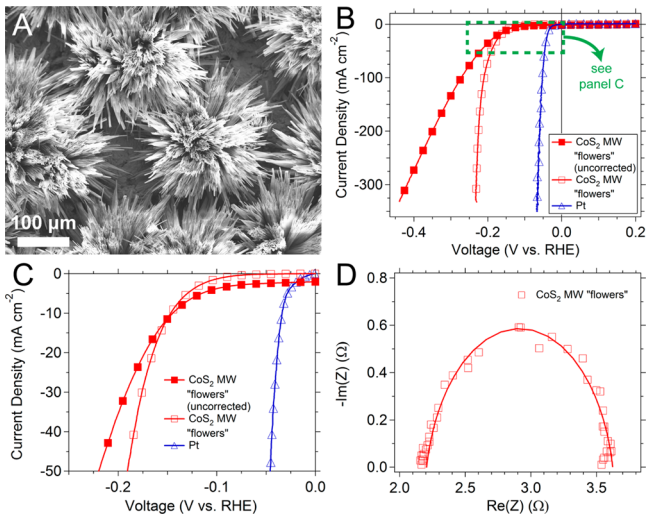

Figure 5. Electrochemical characterization of a hierarchical CoS_2 MW "flower" sample that exhibits high overall catalytic performance toward the HER. (A) SEM image of the CoS_2 MW "flower" electrode. Polarization curves over (B) wider and (C) narrower ranges of applied overpotentials show the high activity of the CoS_2 MW "flower" electrode. (D) Nyquist plot showing the low series and charge transfer resistances of the CoS_2 MW "flower" electrode, with the solid line trace indicating the result of fitting the experimental data to the simplified Randles equivalent circuit inset in Figure 3D.

dx.doi.org/10.1021/ja504099w | J. Am. Chem. Soc. 2014, 136, 10053–10061

details in the Supporting Information). For such a morphology, a high effective electrode surface area leads to high performance (η = −147 mV vs RHE for $J_{cathodic}$ = 10 mA cm^{-2}, which is comparable with the best CoS_2 NW samples), while the MW structures lead to rapid bubble bursting and release from the electrode surface, enabling very high current densities (Figure 5B) and good long-term stability (Figure 4A, orange trace). The uncorrected data in Figure 5B (filled squares) show that cathodic current densities in excess of 300 mA cm^{-2} can be achieved for $\eta_{uncorrected}$ < −420 mV vs RHE, which is practically valuable for the rapid electrocatalytic generation of pure H_2(g). The magnified view of these data in Figure 5C highlights the fact that deviation from the equilibrium potential can result in substantial background current for such high surface area electrodes and that proper treatment of this background is necessary for fair and honest representation of electrode performance (Figure S4, Supporting Information). The EIS data (Figure 5D) show that the operational R_{ct} of this very high performing CoS_2 MW "flower" sample (0.40 Ω cm^2) is consistent with that of the representative CoS_2 film, MW, and NW samples shown in Figure 3D, suggesting that the high overall performance is indeed due to its unique hierarchical morphology.

The significant improvement in the HER catalytic activity of CoS_2 that can be achieved through micro- and nanostructuring suggests that increases in effective surface area could similarly improve CoS_2 as an electrocatalyst for other applications. The convenience with which metallically conducting CoS_2 films, MWs, and NWs can be prepared on glass substrates (Figures 1 and S1, Supporting Information) allows for their facile incorporation into sandwich-style thin-layer liquid-junction solar cells, such as QDSSCs and DSSCs, as the counter electrode. It has recently been shown that CoS_2 films on glass exhibit higher electrocatalytic activity toward polysulfide reduction than Pt films on fluorine-doped tin oxide/glass (FTO/glass) in QDSSCs, enabling improved device performance and stability.[29] Increasing the effective counter electrode surface area through nanostructuring could serve as one pathway for further improving device performance. Figure 6A compares cyclic voltammetry (CV) measurements for sandwich-style thin-layer liquid-junction symmetrical cells assembled with either CoS_2 film or NW electrodes (on glass) and filled with the 2 M Na_2S(aq)/2 M S(aq) sulfide/polysulfide redox electrolyte most commonly used in liquid-junction QDSSCs. The CoS_2 NW electrodes enable vastly increased current densities, and slight shifts in the equilibrium potential even in this highly concentrated electrolyte indicate facile electrode kinetics toward the sulfide/polysulfide redox couple. Additionally, the CoS_2 NW electrodes show good cyclability in the sulfide/polysulfide electrolyte, which suggests long-term stability. The Nyquist impedance plots of these symmetrical cells (Figure 6B) reveal that the CoS_2 NW electrodes exhibit a substantially reduced R_{ct} of 1.72 Ω cm^2 as compared to that of the CoS_2 film electrodes (21.7 Ω cm^2), which is competitive with the 1.61 Ω cm^2 reported for state-of-the-art, high-performance reduced graphene oxide−Cu_2S QDSSC counter electrodes.[44] Interestingly, the CoS_2 NW electrodes also show a lower series resistance (R_s) than the CoS_2 film electrodes (3.74 and 25.3 Ω, respectively), likely owing to the thick conductive CoS_2 film that forms below the NW array (Figure S1, Supporting Information).

Interestingly, we also found metallic CoS_2 to be a highly active electrocatalyst for triiodide reduction and that its

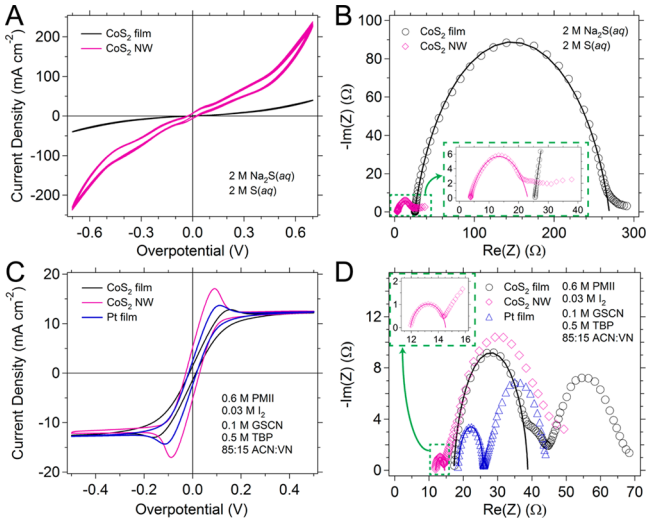

Figure 6. Electrochemical characterization of the activity of CoS_2 film and NW electrodes (on glass) in sandwich-style thin-layer liquid-junction symmetrical cells filled with either (A, B) sulfide/polysulfide or (C, D) iodide/triiodide redox electrolyte. Symmetrical cells were fabricated in parallel using CoS_2 film (black traces and open circle markers) or CoS_2 NW (violet traces and open diamond markers) electrodes (both on glass) and, in the case of the iodide/triiodide symmetrical cells, Pt film on FTO/glass electrodes (blue traces and open triangle markers). The cyclic voltammograms in panel A show 10 complete cycles for each cell, while those in panel C show only the tenth cycle for improved clarity. The main arc of each electrochemical impedance spectrum shown in panels B and D (corresponding to the electrode−electrolyte interface) was fit to the simplified Randles equivalent circuit shown in the inset of Figure 3D, with the results of these fittings indicated as solid traces. The main arc of the CoS_2 NW electrode data, highlighted by a dashed box, is magnified in the insets of panels B and D.

performance can be further enhanced by electrode nanostructuring. To our knowledge, CoS_2 has not been explored as a catalyst for triiodide reduction in DSSCs, even though other cobalt sulfide phases[45−47] and pyrites[48] have been shown to be reasonably effective. The CV characterization of symmetrical cells filled with iodide/triiodide electrolyte shown in Figure 6C reveals that CoS_2 film electrodes do catalyze triiodide reduction, but their performance lags behind that of the Pt on FTO/glass electrodes commonly employed in DSSCs, as indicated by their higher polarization resistance at low overpotential and lower peak current density. The CoS_2 NW electrodes, however, actually surpass the performance of the Pt electrodes, achieving both a lower polarization resistance and higher peak current density. Note that only the tenth CV cycle is shown for each symmetrical cell in Figure 6C for enhanced clarity, but the performance of the CoS_2 electrodes actually increases upon repeated cycling, suggesting high stability in the iodide/triiodide electrolyte (Figure S9, Supporting Information). Furthermore, the EIS Nyquist impedance plots for these symmetrical cells support this performance trend, with the R_{ct} of the CoS_2 NW electrodes (0.232 Ω cm^2) substantially lower than that of the Pt/FTO/glass (0.650 Ω cm^2) and CoS_2 film (1.92 Ω cm^2) electrodes (Figure 6D). Again, the CoS_2 NW on glass electrode exhibits a lower R_s (11.9 Ω) than the CoS_2 film on glass (17.3 Ω) and Pt/FTO/glass electrodes (18.6 Ω) due to the thick conductive CoS_2 layer that forms below the NW array. These electrochemical measurements suggest that not only is CoS_2 a promising replacement for Pt as the cathode

dx.doi.org/10.1021/ja504099w | J. Am. Chem. Soc. 2014, 136, 10053−10061

material in DSSCs, reducing device cost while maintaining performance, but also that nanostructuring of the CoS_2 counter electrode may enable improved performance.

CONCLUSIONS

In summary, we have shown that metallic CoS_2 catalyzes the HER, polysulfide reduction, and triiodide reduction with high efficiency. Further, micro- and nanostructuring of CoS_2 significantly increases its catalytic performance in a synergistic manner: the effective electrode surface area is increased, enabling high current densities at low cathodic overpotentials; simultaneously, micro- and nanostructures facilitate the release of hydrogen gas bubbles from the electrode surface, promoting mechanical stability of the catalyst. Realization of optimized CoS_2 micro- and nanostructuring yields robust electrodes capable of continuously sustaining very high current densities for HER without causing catalyst degradation. These concepts have been further extended to the use of CoS_2 as the catalytic counter electrode material for polysulfide reduction in QDSSCs and triiodide reduction in DSSCs, where nanostructuring of the CoS_2 electrode drastically improves its activity. This has the potential to substantially increase the performance of both QDSSCs and DSSCs while simultaneously eliminating their reliance on precious platinum, increasing their viability as emerging technologies. This work establishes CoS_2 as a general high-performance electrocatalyst for the reduction reactions central to several renewable energy applications and demonstrates the effective strategies of micro- and nanostructuring for improving earth-abundant catalyst materials that may not have the high intrinsic activity of the noble metals.

ASSOCIATED CONTENT

Supporting Information

Experimental details and supporting figures, as noted in the main text. This material is available free of charge via the Internet at http://pubs.acs.org.

AUTHOR INFORMATION

Corresponding Author

jin@chem.wisc.edu

Notes

The authors declare no competing financial interest.

ACKNOWLEDGMENTS

This research is supported by the U.S. Department of Energy, Office of Basic Energy Sciences, Division of Materials Sciences and Engineering, under Award DE-FG02-09ER46664. M.S.F. acknowledges support from the National Science Foundation Graduate Research Fellowship Program. R.D. is grateful for support through a UW−Madison Hilldale Undergraduate Research Fellowship. S.J. thanks the Research Corporation for Science Advancement Scialog Award for Solar Energy Conversion and the UW−Madison H. I. Romnes Faculty Fellowship for support. XPS characterization was performed on instrumentation supported by the UW−Madison College of Engineering, Materials Research Science and Engineering Center (NSF DMR-1121288) and Nanoscale Science and Engineering Center (NSF DMR-0832760).

REFERENCES

(1) Lewis, N. S.; Nocera, D. G. *Proc. Natl. Acad. Sci. U.S.A.* **2006**, *103*, 15729.
(2) Turner, J. A. *Science* **2004**, *305*, 972.
(3) Gray, H. B. *Nat. Chem.* **2009**, *1*, 7.
(4) Walter, M. G.; Warren, E. L.; McKone, J. R.; Boettcher, S. W.; Mi, Q.; Santori, E. A.; Lewis, N. S. *Chem. Rev.* **2010**, *110*, 6446.
(5) Cook, T. R.; Dogutan, D. K.; Reece, S. Y.; Surendranath, Y.; Teets, T. S.; Nocera, D. G. *Chem. Rev.* **2010**, *110*, 6474.
(6) Nocera, D. G. *Acc. Chem. Res.* **2012**, *45*, 767.
(7) McKone, J. R.; Lewis, N. S.; Gray, H. B. *Chem. Mater.* **2014**, *26*, 407.
(8) Nørskov, J. K.; Bligaard, T.; Logadottir, A.; Kitchin, J. R.; Chen, J. G.; Pandelov, S.; Stimming, U. *J. Electrochem. Soc.* **2005**, *152*, J23.
(9) Vesborg, P. C. K.; Jaramillo, T. F. *RSC Adv.* **2012**, *2*, 7933.
(10) Lukowski, M. A.; Daniel, A. S.; Meng, F.; Forticaux, A.; Li, L.; Jin, S. *J. Am. Chem. Soc.* **2013**, *135*, 10274.
(11) Kibsgaard, J.; Chen, Z.; Reinecke, B. N.; Jaramillo, T. F. *Nat. Mater.* **2012**, *11*, 963.
(12) Wang, H.; Lu, Z.; Xu, S.; Kong, D.; Cha, J. J.; Zheng, G.; Hsu, P.-C.; Yan, K.; Bradshaw, D.; Prinz, F. B.; Cui, Y. *Proc. Natl. Acad. Sci. U.S.A.* **2013**, *110*, 19701.
(13) Ding, Q.; Meng, F.; English, C. R.; Cabán-Acevedo, M.; Shearer, M. J.; Liang, D.; Daniel, A. S.; Hamers, R. J.; Jin, S. *J. Am. Chem. Soc.* **2014**, *136*, 8504.
(14) Merki, D.; Fierro, S.; Vrubel, H.; Hu, X. L. *Chem. Sci.* **2011**, *2*, 1262.
(15) Benck, J. D.; Chen, Z. B.; Kuritzky, L. Y.; Forman, A. J.; Jaramillo, T. F. *ACS Catal.* **2012**, *2*, 1916.
(16) Voiry, D.; Yamaguchi, H.; Li, J.; Silva, R.; Alves, D. C. B.; Fujita, T.; Chen, M.; Asefa, T.; Shenoy, V. B.; Eda, G.; Chhowalla, M. *Nat. Mater.* **2013**, *12*, 850.
(17) Lukowski, M. A.; Daniel, A. S.; English, C. R.; Meng, F.; Forticaux, A.; Hamers, R. J.; Jin, S. *Energy Environ. Sci.* Advanced Article, DOI: 10.1039/C4EE01329H.
(18) Popczun, E. J.; McKone, J. R.; Read, C. G.; Biacchi, A. J.; Wiltrout, A. M.; Lewis, N. S.; Schaak, R. E. *J. Am. Chem. Soc.* **2013**, *135*, 9267.
(19) Popczun, E. J.; Read, C. G.; Roske, C. W.; Lewis, N. S.; Schaak, R. E. *Angew. Chem., Int. Ed.* **2014**, *53*, 5427.
(20) McKone, J. R.; Warren, E. L.; Bierman, M. J.; Boettcher, S. W.; Brunschwig, B. S.; Lewis, N. S.; Gray, H. B. *Energy Environ. Sci.* **2011**, *4*, 3573.
(21) McKone, J. R.; Sadtler, B. F.; Werlang, C. A.; Lewis, N. S.; Gray, H. B. *ACS Catal.* **2013**, *3*, 166.
(22) Sun, Y.; Liu, C.; Grauer, D. C.; Yano, J.; Long, J. R.; Yang, P.; Chang, C. J. *J. Am. Chem. Soc.* **2013**, *135*, 17699.
(23) Kong, D.; Cha, J. J.; Wang, H.; Lee, H. R.; Cui, Y. *Energy Environ. Sci.* **2013**, *6*, 3553.
(24) Kong, D. S.; Wang, H. T.; Lu, Z. Y.; Cui, Y. *J. Am. Chem. Soc.* **2014**, *136*, 4897.
(25) Kamat, P. V. *J. Phys. Chem. Lett.* **2013**, *4*, 908.
(26) Selinsky, R. S.; Ding, Q.; Faber, M. S.; Wright, J. C.; Jin, S. *Chem. Soc. Rev.* **2013**, *42*, 2963.
(27) Hagfeldt, A.; Boschloo, G.; Sun, L. C.; Kloo, L.; Pettersson, H. *Chem. Rev.* **2010**, *110*, 6595.
(28) Jaegermann, W.; Tributsch, H. *Prog. Surf. Sci.* **1988**, *29*, 1.
(29) Faber, M. S.; Park, K.; Cabán-Acevedo, M.; Santra, P. K.; Jin, S. *J. Phys. Chem. Lett.* **2013**, *4*, 1843.
(30) Ivanovskaya, A.; Singh, N.; Liu, R.-F.; Kreutzer, H.; Baltrusaitis, J.; Nguyen, T. V.; Metiu, H.; McFarland, E. *Langmuir* **2013**, *29*, 480.
(31) Thio, T.; Bennett, J. W. *Phys. Rev. B* **1994**, *50*, 10574.
(32) Cabán-Acevedo, M.; Faber, M. S.; Tan, Y. Z.; Hamers, R. J.; Jin, S. *Nano Lett.* **2012**, *12*, 1977.
(33) Cabán-Acevedo, M.; Liang, D.; Chew, K. S.; DeGrave, J. P.; Kaiser, N. S.; Jin, S. *ACS Nano* **2013**, *7*, 1731.
(34) Zhu, L.; Susac, D.; Teo, M.; Wong, K. C.; Wong, P. C.; Parsons, R. R.; Bizzotto, D.; Mitchell, K. A. R.; Campbell, S. A. *J. Catal.* **2008**, *258*, 235.
(35) Jirkovský, J. S.; Björling, A.; Ahlberg, E. *J. Phys. Chem. C* **2012**, *116*, 24436.
(36) Zhao, C.; Li, D.; Feng, Y. *J. Mater. Chem. A* **2013**, *1*, 5741.

(37) Harrison, J. A.; Kuhn, A. T. *Surf. Technol.* **1983**, *19*, 249.
(38) Li, Y.; Tan, B.; Wu, Y. *J. Am. Chem. Soc.* **2006**, *128*, 14258.
(39) Li, Y.; Wu, Y. *Chem. Mater.* **2010**, *22*, 5537.
(40) Xia, X.; Chao, D.; Qi, X.; Xiong, Q.; Zhang, Y.; Tu, J.; Zhang, H.; Fan, H. J. *Nano Lett.* **2013**, *13*, 4562.
(41) Meng, F.; Morin, S. A.; Forticaux, A.; Jin, S. *Acc. Chem. Res.* **2013**, *46*, 1616.
(42) van der Heide, H.; Hemmel, R.; van Bruggen, C. F.; Haas, C. *J. Solid State Chem.* **1980**, *33*, 17.
(43) Wang, J.; Zheng, Y.; Nie, F.-Q.; Zhai, J.; Jiang, L. *Langmuir* **2009**, *25*, 14129.
(44) Radich, J. G.; Dwyer, R.; Kamat, P. V. *J. Phys. Chem. Lett.* **2011**, *2*, 2453.
(45) Wang, M.; Anghel, A. M.; Marsan, B.; Ha, N.-L. C.; Pootrakulchote, N.; Zakeeruddin, S. M.; Grätzel, M. *J. Am. Chem. Soc.* **2009**, *131*, 15976.
(46) Kung, C.-W.; Chen, H.-W.; Lin, C.-Y.; Huang, K.-C.; Vittal, R.; Ho, K.-C. *ACS Nano* **2012**, *6*, 7016.
(47) Chang, S.-H.; Lu, M.-D.; Tung, Y.-L.; Tuan, H.-Y. *ACS Nano* **2013**, *7*, 9443.
(48) Huang, Q.-H.; Ling, T.; Qiao, S.-Z.; Du, X.-W. *J. Mater. Chem. A* **2013**, *1*, 11828.